Flexible Nanocomposite Generator Made of BaTiO₃ Nanoparticles and Graphitic Carbons

Kwi-Il Park, Minbaek Lee, Ying Liu, San Moon, Geon-Tae Hwang, Guang Zhu,
Ji Eun Kim, Sang Ouk Kim, Do Kyung Kim, Zhong Lin Wang, and Keon Jae Lee*

While global energy consumption has steadily increased in the past decades due to industrialization and population growth,[1] society is facing a problem with the depletion of fossil energy resources as well as environmental problems (such as global warming, carbon dioxide emissions, and damage to the ozone layer).[2] These challenges can be addressed by renewable energy resources, which are always available everywhere.[1,2] Outdoor renewable energy sources such as solar energy (15 000 $\mu W/cm^3$),[3,4] wind energy (380 $\mu W/cm^3$),[5] and wave energy (1 000 W/cm of wave crest length)[6,7] can provide large-scale needs of power. However, for driving small electronics in indoor or concealed environments[3,8] (such as in tunnels, clothes, and artificial skin) and implantable biomedical devices, innovative approaches have to be developed.

One way of energy harvesting without such restraints is to utilize piezoelectric materials that can convert vibrational and mechanical energy sources from human activities such as pressure, bending, and stretching motions into electrical energy.[9–11] Wang and co-workers[9,10,12–15] have used piezoelectric ZnO nanowire arrays to develop a nanogenerator technologies, who have demonstrated the feasibility using this type of generator to power commercial light-emitting diodes (LEDs),[13] liquid crystal displays,[14] and wireless data transmission.[15] These nanogenerators can also convert tiny bits of biomechanical energy (from sources such as the movement of the diaphragm, the relaxation and contraction of muscle, heartbeat, and the circulation of blood) into power sources.[16,17]

Recently, there have been attempts to fabricate thin film-type nanogenerators[11,18] with perovskite ceramic materials ($PbZr_xTi_{1-x}O_3$ and $BaTiO_3$), which have a high level of inherent piezoelectric properties. The $BaTiO_3$ thin film nanogenerator has demonstrated by the authors[11] using the transfer process[19–22] of high temperature annealed perovskite thin film from bulk substrates onto flexible substrates; it generates a much higher level of power density than other devices with a similar structure.[10]

Herein, we report the nanocomposite generator (NCG) achieving a simple, low-cost, and large area fabrication based on $BaTiO_3$ nanoparticles (NPs) synthesized via a hydrothermal reaction (see Method S1)[23] and graphitic carbons, such as single-walled and multi-walled carbon nanotubes (SW/MW-CNTs), and reduced graphene oxide (RGO). The $BaTiO_3$ NPs and carbon nanomaterials are dispersed in polydimethylsiloxane (PDMS) by mechanical agitation to produce a piezoelectric nanocomposite (p-NC). The p-NC is spin-casted onto metal-coated plastic substrates and cured in an oven. Under periodic external mechanical deformation by bending stage or biomechanical movements from finger/feet of human body, electric signals are repeatedly generated from the NCG device and used to operate a commercial red LED.

The schematic diagrams of the fabrication process are shown in **Figure 1**a and detail information described in Experimental section. Figures 1b and c show cross-sectional scanning electron microscopy (SEM) images of a 250 μm thick p-NC that is sandwiched between the top and bottom metal-coated plastic substrates. A magnified cross-sectional SEM image (Figure 1c) shows that the $BaTiO_3$ NPs and the MW-CNTs are well distributed in the PDMS matrix. The $BaTiO_3$ NPs generate piezoelectric potential under external stress and act as an energy generation source. The CNT's role in an NCG device as dispersant, stress reinforcing agent, and conducting functional material is explained later. The volume percentage of CNT is controlled so low so that they do not affect the dielectric property of the entire structure. The hydrothermal $BaTiO_3$ NPs have a rounded shape with size of 100 nm (see Figure 1d and Figure S1a-i). Raman analysis is conducted to provide a more comprehensive phase characterization of the $BaTiO_3$ NPs (the inset of Figure 1d). The sharpness of the spectrum in the range of 305 to 720 cm^{-1} is ascribed to the A_1 and E (longitudinal optical) modes, which are specific to a tetragonal phase of $BaTiO_3$.[24] The crystalline structure of the $BaTiO_3$ NPs is characterized by X-ray diffraction (see Figure S1a-ii). The Raman shift and X-ray diffraction pattern indicate that the $BaTiO_3$ NPs have good crystallinity with an excellent ferroelectric tetragonal phase. The MW-CNTs (Carbon Nano-material Tech. Co.), which are prepared via catalyst chemical vapor deposition, have a diameter of 5 to 20 nm and a length of ~10 μm (see TEM images of Figure S1b-i). We also employed the SW-CNTs with a diameter of ~3 nm and RGO obtained by modified Hummers methods[25] (see Method S2) to confirm the universality of carbon nanomaterials in energy generation behavior (see Figures S1c and S1d). The photograph in Figure 1f shows the core p-NC material stretched by

K.-I. Park, S. Moon, G.-T. Hwang, J. E. Kim,
Prof. S. O. Kim, Prof. D. K. Kim, Prof. K. J. Lee
Department of Materials Science and Engineering
Korea Advanced Institute of Science
and Technology (KAIST)
291 Daehak-ro, Yuseong-gu, Daejeon, 305-701
Republic of Korea
E-mail: keonlee@kaist.ac.kr
Dr. M. Lee, Y. Liu, G. Zhu, Prof. Z. L. Wang
School of Materials Science and Engineering
Georgia Institute of Technology
771 Ferst drive, Atlanta, Georgia, 30332-0245, USA

COMMUNICATION
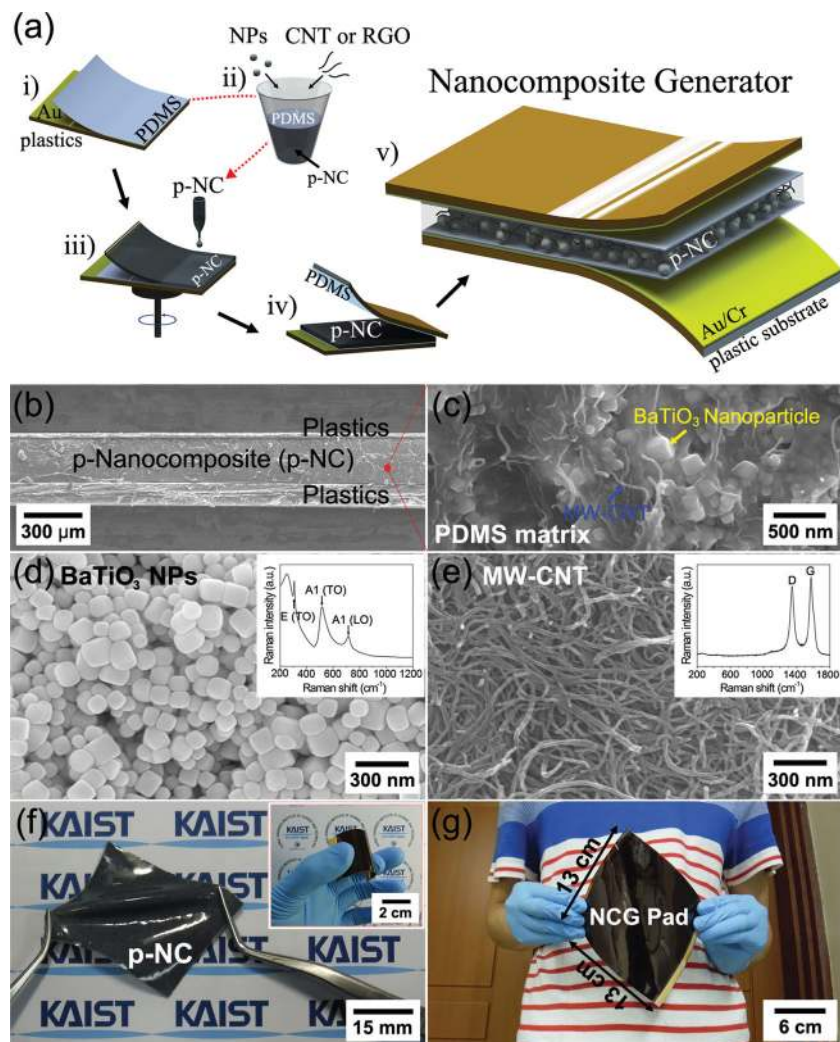
Figure 1. (a) Schematic illustration of the process for fabricating NCG device. (b) A cross-sectional SEM image of an NCG device. (c) A magnified cross-sectional SEM photograph of the p-NC. (d) A SEM image of the $BaTiO_3$ NPs synthesized by hydrothermal method. The inset shows a Raman spectrum obtained from and $BaTiO_3$ NPs. (e) The MW-CNTs have a diameter of 20 nm and a length of 2 μm. The inset shows a typical Raman shift of the MW-CNTs with large D bands. (f) Photograph of the p-NC stretched by tweezers. The inset shows the NCG device (3 cm x 4 cm) bent by fingers. (g) A large-area type NCG device (13 cm x 13 cm) fabricated by spin-casting or Mylar bar-coating.

tweezers; the inset shows a completely bended NCG device on metal-coated flexible substrates. These images confirm that the nanocomposites that generate self-powered energy are very flexible, bendable, and even stretchable (see Video S1). A large area NCG device (NCG pad, 13 cm x 13 cm) can also be fabricated by a process of spin-casting or Mylar bar-coating[26] (Figure 1g). We believe that this arbitrary scalability to a large area fabrication is a unique advantages over previous nanogenerator techniques[10] because it overcomes the size limitation caused by the high vacuum chamber growth. The thickness can also be easily adjusted by multiple spin-casting or simple die casting (see Figures S2 and S3).

We measured the generated outputs of the NCG device during the periodic bending and unbending motion of the bending stage; the results are shown in **Figure 2**. To exclude any artifact from the external electrostatic charges, the sample is placed in a Faraday cage on an optical table and bending system is well grounded. The measured output voltage and current (Figure 2b) correspond to the three states of the NCG device shown in Figure 2a: that is, the original state, the bending state, and the release state. To verify that the measured output signals are purely generated by the NCG sample, we conduct a widely used switching-polarity test.[11,12] When a measurement instrument is forward connected to the device (corresponding to the upper inset of Figure 2b-i), the NCG device generates a positive voltage and current upon the bending states (Figures 2b-i and ii). In the case of the reverse connection (to the upper inset of Figure 2c-i), the negative output pulses are measured. The results indicate that the measured outputs are the true signals generated from our NCGs strained by bending motions. Under the continual bending and unbending cycles, the NCG device repeatedly generates an open-circuit voltage (V_{oc}) of ~3.2 V and a short-circuit current (I_{sc}) signal of 250 to 350 nA; these output values are produced for a maximum horizontal displacement of 5 mm from an original 4 cm long sample at a deformation rate of 0.2 m·s^{-1} (see Video S1 for real-time live views of the energy harvesting). The amplitude of the output voltage generated from the NCG device increases from 0.2 V to 3.2 V after the poling process (see Figure S4), and also depends on the composition of nanomaterials (Figure S5 and Table S1), the angular bending strain (Figure S6), and strain rate (Figure S7). The durability test is conducted to confirm the mechanical stability of the NCG device (Figure 2d). The voltage amplitude does not appear to have changed significantly after 1200 bending cycles (more than 1 hour of operation). The NCG device also shows superior mechanical stability during 600 bending cycles after 3 and 7 days of testing. The bottom insets of Figure 2d show the magnified output signals (see Figure S8 for the durability test result of the current signals).

The detail power generation mechanism of the NCG device is described in Figure S9. In addition, we calculate the piezopotential distributions inside the NCG by using a simple rectangular model composed of six $BaTiO_3$ NPs in a PDMS matrix (see Method S3) as shown in **Figure 3**a and b. The material parameters of the $BaTiO_3$ and PDMS, which are taken from the COMSOL simulation software, are used for the finite element analysis.[27] When the three-layer structure comprised of a top thin plastic substrate, a layer of six $BaTiO_3$ NPs-embedded PDMS, and a bottom thick plastic substrate is bent, the tensile stress is built-up over the entire PDMS matrix due to the shift
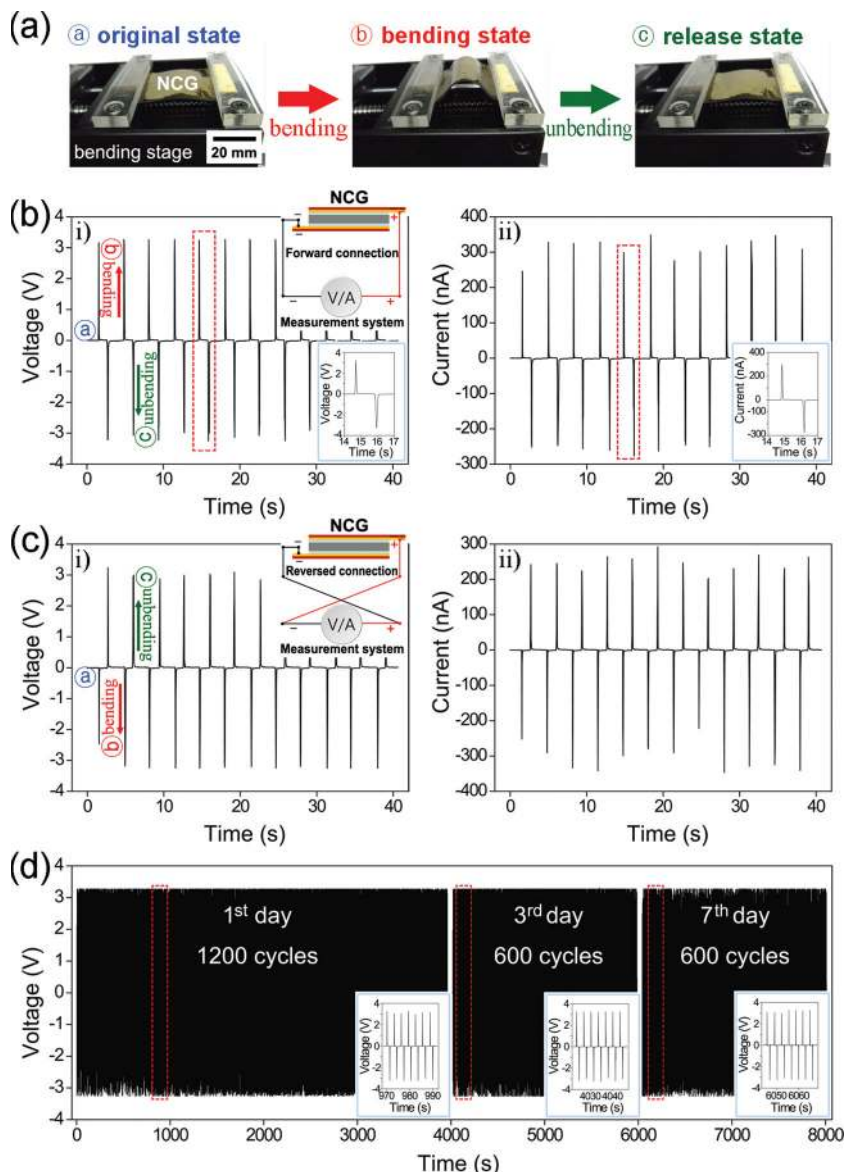
Figure 2. (a) Optical images of NCG devices in their original, bending, and release states. (b) The measured output voltage and current signals of the NCG device in the forward connection during the periodic bending and unbending motions. (c) The open-circuit voltage and short-circuit current signals generated in the reverse connection. (d) The durability test results conducted to confirm the mechanical stability of the NCG device.

dispersion (the schematics of Figure 4a-i); thus, they lead to the low output voltage (Figure 4b-i). In the case of the NCG devices with carbon nanomaterials (Figures 4a-ii and 1c), the BaTiO$_3$ NPs can be well distributed by forming a complex mixture with CNT networks; as a results, a high output voltage is generated (Figure 4b-ii). The above theories are well supported by the comparative results of the measured output voltage of devices with and without CNT networks (Figures 4b-i and ii). We also calculated the piezopotential distribution of the aggregated NP model (Figure 4a-iii). The piezopotential of the aggregated NP model is inferior to that of a well-distributed NP model (Figures 3a and b) that is consistent with our assertions. Another role of CNT is to reinforce the stress applied to NPs by enhancing the composite stress; the enhancement is attributed to a change in the mechanical property of the composites material.[28,29] Since the CNTs are well mixed and entangled with NPs in PDMS matrix, the small NPs can significantly be stressed. This phenomenon is depicted in the schematic illustrations of Figures 4a-iv and 4a-v. The calculation of the piezopotential distribution of the CNT-reinforced model is based on the modified parameters[30] of the PDMS that is affected by the addition of CNTs (Figure 4a-vi). In accordance with our initial assumption, the piezopotential difference of the reinforced model is higher than that of the non-CNT model (Figures 3 and b). Finally, the conduction paths formed by the CNT networks can reduce the internal resistance of NCG devices[31] and thus the resistance, yielding the short voltage lifetime and the high output characteristics.[32,33] As shown in the bottom-right insets of Figures 4b-i and ii, the NCG device generates a sharper voltage peak compared to the device with only NPs. The equivalent circuits of the NCG device are depicted in the bottom-left inset of Figure 4b-i, where R$_N$, C$_N$, and R$_L$ are the internal NCG resistance, the NCG capacitance, and the load resistance of the measurement system (M/S), respectively. The piezoelectric potentials are generated by the mechanical deformation and subsequently removed during the RC discharging process with a time constant (τ) according to the equation (1).[32]

$$\tau = (R_N + R_L) \cdot C_N \qquad (1)$$

The NCG device shows a shorter output voltage lifetime (50.29 ms), which is defined as full width at half maximum (FWHM) of the voltage peak, than that (71.51 ms) of the device without CNTs (see the Figure S10 and Table S1 for the details of voltage lifetime calculated from the voltage-time plots). It indicates that a short lifetime of NCG device caused by CNT

of the neutral plane to bottom side. Figure 3b shows the color-coded piezopotential distribution of the PDMS between the top and bottom electrodes. The calculated piezopotential for tensile strain of 0.33% in the X-axis is generated across the top and bottom sides of the PDMS matrix by the piezoelectric NPs.
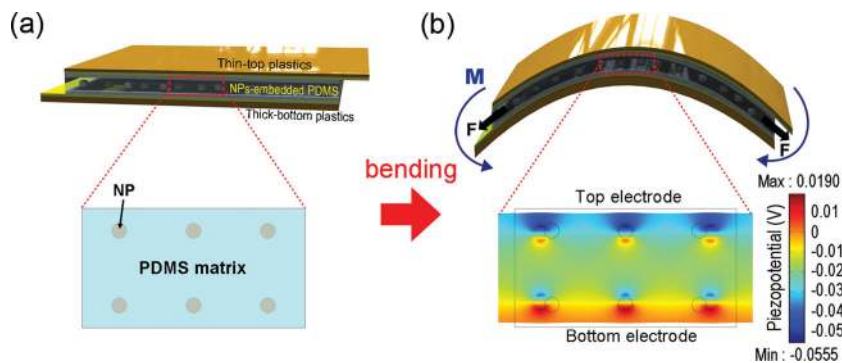
We characterized the NCG device without any CNTs in order to exploit the role of the CNTs within the device. The characterization is supported by the calculated piezopotential and measurement results (**Figures 4**a and b). It is a challenging task to disperse BaTiO$_3$ NPs uniformly inside the composite for a high-performance NCG device. Only the BaTiO$_3$ NPs in the PDMS matrix cannot avoid the aggregation and poor

COMMUNICATION

Figure 3. (a) Simulation model of a NCG device. The entire structure includes the six BaTiO$_3$ NPs-embedded PDMS between the top and bottom plastic substrate. (b) The simulated piezo-potential difference inside the PDMS between top and bottom electrodes indicated by color code.

additions leads to increasing the output voltage. The PDMS sample with only MW-CNTs is also characterized and compared to other devices to confirm that the measured outputs are generated from piezoelectric NPs (see Figure S11a). No reliable signals are observed upon bending and unbending motions. This result indicates that the output signals of NCG device are obtained from charges generated by piezo-electric NPs.

The NCG devices with SW-CNTs and RGO are fabricated and characterized to study the electric and geometric effects of other graphitic carbon nanomaterials instead of the MW-CNTs (see Figure S12). The NCG device that contains the nanomaterials of the SW-CNTs and BaTiO$_3$ NPs generates an output voltage of ~3.2 V, which is similar to that of the MW-CNT-based NCG device shown in Figure 4b-ii. The similarity indicates that the electrical properties of CNT have an insignificant influence on outputs of an NCG device. Unlike the high performance of MW/SW-CNT-based devices, the NCG device with RGO produces a lower output voltage (~2.0 V) than a CNT-based NCG device. This distinction is likely due to the difference in the degree of mixing, which in turn is caused by the geometrical difference between the CNT networks and the laminated RGO structures.

We demonstrated the energy harvesting which converts human muscle movement into electrical energy (Figure S13). The small-scaled device and NCG pad are driven by the slight bending motions of finger tapping and regular foot stepping, respectively. The voltage and current produced by the slow finger motion reaches up to ~200 mV and ~7 nA, respectively (see Figure S13b and Video S1); the output values by finger tapping are lower than those of bending stage with high speed deformation of Figure 2. The NCG pad repeatedly generates the output signals of ~1.5 V
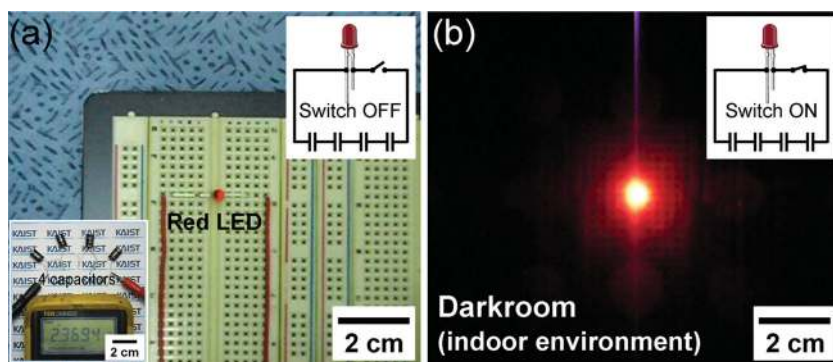
and ~150 nA (see Figure S13d and Video S1); these output values are produced from an activation area of 5 cm x 7 cm with applying force of ~200 N (i.e., ~57 kPa).

For a potential utilization of our energy harvesting technology, we demonstrated the lit up of a commercial LED solely with the electricity generated from the NCG device. As shown in Figure S14a, the NCG device is connected to a predesigned circuit composed of diodes and capacitors; it is activated by bending and unbending motions for ~1 hr (2.5 Hz) to accomplish the energy storage process. The alternating energy sources are rectified (Figures S14b and S14c) and simultaneously stored in the four capacitors in parallel. The voltage charged to a single capacitor is ~0.6 V, which is lower than the peak output voltage of NCG devices due to voltage drop drained by the rectifying circuits or the capacitor leakage.[13] The total output voltage of the four charged capacitors aligned in serial alignment reaches up to ~2.37 V, which is sufficient to drive a commercial LED. **Figure 5**a shows the captured image of a red LED integrated into the circuit shown in the top inset. When
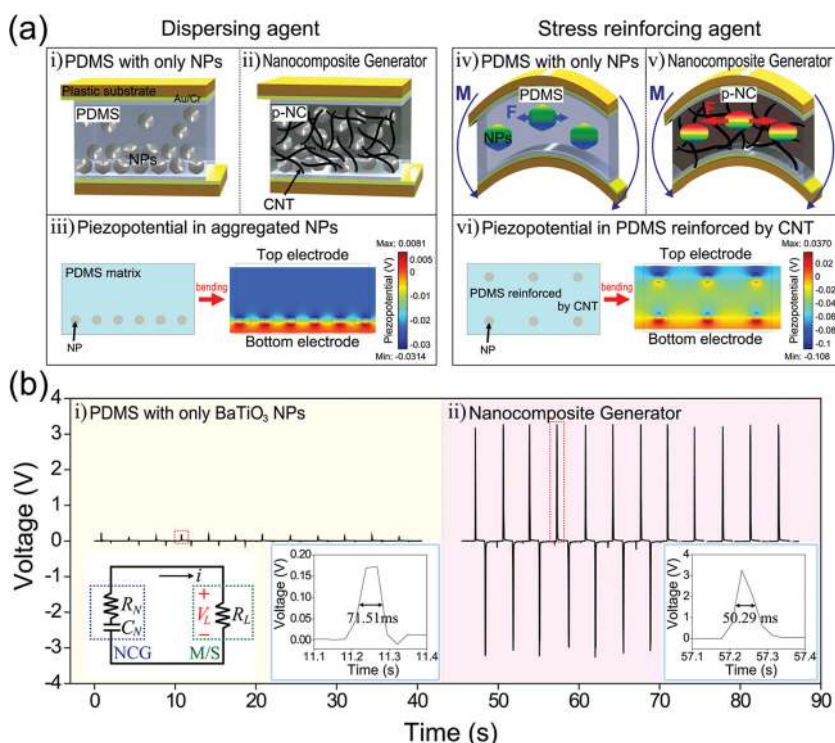
Figure 4. (a) Schematics of the cross-sectional structure of NCG devices and the calculated piezopotential distributions for explaining the role of CNTs. The CNTs act as dispersing (ii) and stress reinforcing agents (v) which are well supported by the calculated piezopotential difference (iii and vi). (b) The output voltages generated from a device containing only BaTiO$_3$ NPs and a NCG device. The good distribution of NPs and stress enhancement by CNTs lead to the superior output voltage. The bottom-right insets show the magnified output voltage generated by the mechanical bending motion. The bottom-left inset of shows the equivalent circuit of NCG devices.

Materials
Views
www.MaterialsViews.com

ADVANCED
MATERIALS
www.advmat.de

COMMUNICATION

Figure 5. (a) A captured image of a commercial red LED incorporated into the circuit. The bottom inset shows the measured voltage (~2.37 V) when the four capacitors are aligned in a serial. (b) A captured photograph showing an LED lit up by the electric energy generated from an NCG device.

Information for a video clip on the production process of p-NC, Video S1).

Spin-casting of the p-NC layer: The p-NC is spin-casted onto PDMS/Au/Cr/plastic substrates at a spinning rate of 1500 rpm for 30 sec and cured at 85 °C for 5 min in an oven.

Fabrication of the NCG: Another top PDMS/metal-coated plastic substrate is placed in uniform contact with a p-NC/PDMS/metal-coated bottom flexible substrate and fully cured at room temperature for 1 day. Finally, the NCG device is poled at 150 °C by applying an electric field of 100 kV/cm for 20 hr. The fabricated NCG device maintains mechanical stability up to an extreme bending radius of 0.8 cm for many bending cycles. The Cu wires are attached to metal pads by means of silver (Ag) paste for the characterization of the output voltage and current signals.

the switch is turned on (the inset of Figure 5b), the LED is lit up and lasted for ~3 s (Figure 5b) (see Video S1 for a video clip of the LED being lit up by the electricity generated from the NCG device). The commercial microelectronic LED is successfully operated by the piezoelectric energy from the NCG device without any external electric power source.

In summary, we have fabricated the NCG device based on piezoelectric BaTiO$_3$ NPs and universal graphitic carbons. The BaTiO$_3$ NPs are mixed with one of carbon nanomaterials (SW/MW-CNTs and RGO) to prepare the p-NC. The NCG devices obtained by spin-casting/bar-coating method convert the mechanical deformation and even tiny biomechanical movements into electric energy. We have theoretically analyzed the principle of power generation and CNT's role in NCG device, which have been supported by the finite element simulation. The alternating energy generated from an NCG device is stored in capacitors and subsequently used to turn on a commercial LED device. Our p-NC technique successfully overcomes the size-related restrictions existed in previous nanogenerator and enables simple, low-cost, and large-scale self-powered energy system. This result innovatively expands the feasibility of self-powered energy systems for application in consumer electronics, sensor networks, and energy harvesting in indoor environments.

Experimental Section

Spin-casting of the dielectric layer onto the metal-coated plastic substrates: Radio frequency magnetron sputtering is used to deposit layers of Cr (10 nm) and Au (100 nm) onto flexible substrates (Kapton film, 25 μm and 125 μm in thickness) for the top and bottom electrodes. A layer of PDMS (Sylgard 184, Dow Corning) is spin-casted onto Au/Cr/plastic substrates to form a dielectric layer and then cured at 85 °C for 10 min in an oven.

Production of the p-NC: The BaTiO$_3$ NPs are prepared via hydrothermal reactions at 200 °C for 24 hr. They are mixed with a graphitic carbon (either SW/MW-CNTs or RGO) in specific proportions (the compositional details of which are shown in Table S1 of the Supporting Information). The mixture is then stirred for ~5 hr in ethanol with a magnetic bar. After the subsequent drying and granulation, the well-mixed nanomaterials (compositions of 1 wt% MW-CNTs and 12 wt% BaTiO$_3$ NPs) are poured into a PDMS matrix for the final p-NC product (see the Supporting

Supporting Information

Supporting Information is available from the Wiley Online Library or from the author.

[1] G. J. Aubrecht, *Energy: Physical, Environmental, and Social Impact*, Pearson Education, London **2006**.

[2] C. Beggs, *Energy: Management, Supply and Conservation*, Elsevier, Oxford **2002**.

[3] S. Priya, D. J. Inman, *Energy Harvesting Technologies*, Springer Science, New York, **2009**.

[4] S. Roundy, P. K. Wright, J. Rabaey, *J. Comput. Commun.* **2003**, *26*, 1131.

[5] S. Roundy, E. S. Leland, J. Baker, E. Carleton, E. Reilly, E. Lai, B. Otis, J. M. Rabaey, P. K. Wright, V. Sundararajan, *IEEE Pervas. Comput.* **2005**, *4*, 28.

[6] K. Rhinefrank, presented at Energy Ocean 2005, April 26–28, Washington, DC.

[7] US Department of the Interior (Minerals Management Service), Technology White Paper on Wave Energy Potential on the US Outer Continental Shelf, 2006. (http://ocsenergy.anl.gov/documents/docs/OCS_EIS_WhitePaper_Wave.pdf).

[8] Y. Qi, M. C. McAlpine, *Energy Environ. Sci.* **2010**, *3*, 1275.

[9] Z. L. Wang, J. H. Song, *Science* **2006**, *312*, 242.

[10] S. Xu, Y. Qin, C. Xu, Y. G. Wei, R. S. Yang, Z. L. Wang, *Nat. Nanotechnol.* **2010**, *5*, 366.

[11] K. I. Park, S. Xu, Y. Liu, G. T. Hwang, S. J. L. Kang, Z. L. Wang, K. J. Lee, *Nano Lett.* **2010**, *10*, 4939.

[12] R. S. Yang, Y. Qin, L. M. Dai, Z. L. Wang, *Nat. Nanotechnol.* **2009**, *4*, 34.

[13] G. Zhu, R. Yang, S. Wang, Z. L. Wang, *Nano Lett.* **2010**, *10*, 3151.

[14] Y. Hu, Y. Zhang, C. Xu, G. Zhu, Z. L. Wang, *Nano Lett.* **2010**, *10*, 5025.

[15] Y. Hu, Y. Zhang, C. Xu, L. Lin, R. L. Snyder, Z. L. Wang, *Nano Lett.* **2011**, *11*, 2572.

[16] R. Yang, Y. Qin, C. Li, G. Zhu, Z. L. Wang, *Nano Lett.* **2009**, *9*, 1201.

[17] Z. Li, G. A. Zhu, R. S. Yang, A. C. Wang, Z. L. Wang, *Adv. Mater.* **2010**, *22*, 2534.

[18] Y. Qi, J. Kim, T. D. Nguyen, B. Lisko, P. K. Purohit, M. C. McAlpine, *Nano Lett.* **2011**, *11*, 1331.

[19] K. I. Park, S. Y. Lee, S. Kim, J. Chang, S. J. L. Kang, K. J. Lee, *Electrochem. Solid-State Lett.* **2010**, *13*, G57.

[20] S. Kim, H. Y. Jeong, S. K. Kim, S.-Y. Choi, K. J. Lee, *Nano Lett.* **2011**, *11*, 5438.

[21] S. Y. Lee, K. I. Park, C. Huh, M. Koo, H. G. Yoo, S. Kim, C. S. Ah, G. Y. Sung, K. J. Lee, *Nano Energy* **2011**, *1*, 145.

[22] M. Koo, S. Y. Park, K. J. Lee, *Nanobiosensors in Disease Diagnosis* **2012**, *1*, 5.

[23] D. R. Chen, X. L. Jiao, *J. Am. Ceram. Soc.* **2000**, *83*, 2637.

[24] A. D. Li, C. Z. Ge, P. Lu, D. Wu, S. B. Xiong, N. B. Ming, *Appl. Phys. Lett.* **1997**, *70*, 1616.

[25] J. E. Kim, T. H. Han, S. H. Lee, J. Y. Kim, C. W. Ahn, J. M. Yun, S. O. Kim, *Angew. Chem. Int. Edit.* **2011**, *50*, 3043.

[26] K. J. Lee, M. J. Motala, M. A. Meitl, W. R. Childs, E. Menard, A. K. Shim, J. A. Rogers, R. G. Nuzzo, *Adv. Mater.* **2005**, *17*, 2332.

[27] D. Armani, C. L. Liu, N. Aluru, Twelfth IEEE International Conference on Micro Electro Mechanical Systems, January 17–21, **1999**, Orlando, USA, p. 222.

[28] J. Suhr, N. Koratkar, P. Keblinski, P. Ajayan, *Nat. Mater.* **2005**, *4*, 134.

[29] V. P. Veedu, A. Y. Cao, X. S. Li, K. G. Ma, C. Soldano, S. Kar, P. M. Ajayan, M. N. Ghasemi-Nejhad, *Nat. Mater.* **2006**, *5*, 457.

[30] L. Ci, J. Suhr, V. Pushparaj, X. Zhang, P. M. Ajayan, *Nano Lett.* **2008**, *8*, 2762.

[31] C. Seoul, Y. T. Kim, C. K. Baek, *J. Polymer. Sci. Part B* **2003**, *41*, 1572.

[32] C. Chang, Y.-K. Fuh, L. Lin, Solid-State Sensors, Actuators and Microsystems Conference (Transducers), June 21–25, **2009**, Denver, USA, p.1485.

[33] C. E. Chang, V. H. Tran, J. B. Wang, Y. K. Fuh, L. W. Lin, *Nano Lett.* **2010**, *10*, 726.

Supporting Information for:

Flexible Nanocomposite Generator Made of BaTiO₃ Nanoparticles and Graphitic Carbons

By Kwi-Il Park, Minbaek Lee, Ying Liu, San Moon, Geon-Tae Hwang, Guang Zhu, Ji Eun Kim, Sang Ouk Kim, Do Kyung Kim, Zhong Lin Wang, and Keon Jae Lee*

[*] Prof. K. J. Lee, K.-I. Park, S. Moon, G.-T. Hwang, J. E. Kim, Prof. S. O. Kim, Prof. D. K. Kim
Department of Materials Science and Engineering, Korea Advanced Institute of Science and Technology (KAIST)
291 Daehak-ro, Yuseong-gu, Daejeon, 305-701 (Republic of Korea)
E-mail: keonlee@kaist.ac.kr

   Prof. Z. L. Wang, Dr. M. Lee, Y. Liu, G. Zhu
School of Materials Science and Engineering, Georgia Institute of Technology
771 Ferst drive, Atlanta, Georgia, 30332-0245 (United States)

This PDF file includes:

Methods S1 to S3

Figures S1 to S14

Tables S1 and S2

Other Supporting Online Material for this manuscript

Video S1

Methods

Method S1. Synthesis of $BaTiO_3$ nanoparticles

Ti precursors are prepared by means of a hydrolysis reaction of Ti-butoxide ($Ti[O(CH_2)_3 \cdot CH_3]_4$, reagent grade 97 %, Aldrich Chemical Co.). The Ti-butoxide (0.025 mol) is diluted with 5 mL ethanol (C_2H_5OH, 99.8 %, Samchun Chemicals Co.) and 5 mL of deionized water. A 4 mL solution of ammonia is then added to the mixture. For the preparation of $BaTiO_3$ powders, the solutions are dispersed with magnetic stirring at 80 ºC. This step is followed by the addition of a 10 mL solution of 37.5 M barium hydroxide monohydrate ($Ba(OH) \cdot 2H_2O$, 98 %, Aldrich Chemical Co.). The final suspension that created a Ba/Ti molar ratio of 1.5:1 is transferred to a 100 mL Teflon-lined stainless-steel autoclave with a fill factor of 60 %. The autoclave is heated to 200 ºC for 24 hr and then cooled to room temperature. The resultant products are filtered and washed 5 times with distilled water and ethanol, and then dried in air at 80 ºC for 24 hr.

**Method S2.** Preparation of reduced graphene oxide (RGO)

Graphene oxide (GO) is created using the modified Hummers methods from the commercially available graphite sources (flake type: batch # 52996AJ, Sigma Aldrich Co.). The graphite (1 g) is oxygenated in 40 mL of sulfuric acid (H_2SO_4, Merck Co.). Then, 3.5 g of potassium permanganate ($KMnO_4$, Sigma Aldrich Co.) is slowly added at 35 ºC. For sufficient oxygenation, the reaction mixture is stirred for 24 hr with nitrogen a (N_2) purge. After the completion of the oxygenation, the excess water and 35% of the H_2O_2 are added to the reaction mixture. The resultant 2 g of GO powder is thoroughly filtered and washed 5 times with 1M of an HCl solution and deionized water; it is then redispersed in 1 L of deionized water. The GO dispersion (~2 wt%) is put in the a water bath ultrasonicator (Branson 5510) for 30 min for monolayer exfoliation. The GO dispersion that is sealed in a dialysis membrane (Spectra/Por Dialysis Membrane MWCO: 6-8000) is submerged in deionized water and stirred for 3 days. A fully exfoliated GO dispersion is obtained when the supernatant and unexfoliated GO are removed by centrifugal separation. The final step of the RGO preparation involves a process of annealing the GO solution in a tube furnace at 700 ºC for 1 hr in N_2.

Method S3. Details for Modeling and Calculation

The distance between each geometry center of three layers (top plastic, p-NC, and bottom plastic) and the neutral plane are y_1, y_2 and y_3, from up to down. From the definition of neutral plane, $E_1T_1y_1+E_2T_2y_2+E_3T_3y_3=0$, where E and T are a young's modulus and thicknesses, respectively. The contribution of the PDMS layer is negligible, because the modulus of plastic substrate (2.5 GPa) is much larger than that of PDMS (1 MPa). As y_1-y_3 = 450 μm, T_1 = 25 μm, T_2 = 375 μm, and y_3 = -28 μm, the neutral plane is 28 μm above the center and 159.5 μm below the surface of the plastic substrates. Thus, the p-NC is located above the neutral plane, which results in solely tensile stress during bending process. The finite element analysis (FEA) is conducted for a few particles in the key polymer layer. The p-NC deformed by the tensile strain of 0.33% exhibited the distribution of strain varying from ~0.2 % to ~0.5 %. The parameters (E = 750 kPa, shear modulus of G = 250 kPa, density of 1 g/cm^3) of PDMS are obtained from ref 44. In the case of NP, a young's modulus of 67 GPa and a piezoelectric coefficient (d_{33}) of 190 pC/N are taken from COMSOL software and its density of 5.7 g/cm^3 is measured by pycnometer. For the calculation of a piezopotential distribution in CNT-reinforced model, we double the young's modulus of CNT-PDMS composite, which increases the stress in the NPs and enhances the output voltage under the same bending condition. The dielectric constant of the PDMS layer can be changed by the electrical properties of CNTs, resulting in the unexpected influence on output voltage simulation. This effect, however, could be cancelled out by electrical leakage since CNTs have high electrical conductivity. Our calculation is valid when the volume percentage of the added CNT is low value below 1 %.

Figures and Tables

1. Transmission electron microscope (TEM) images, X-ray diffraction (XRD) patterns, and Raman spectra of BaTiO₃ nanoparticles (NPs) and graphitic carbons
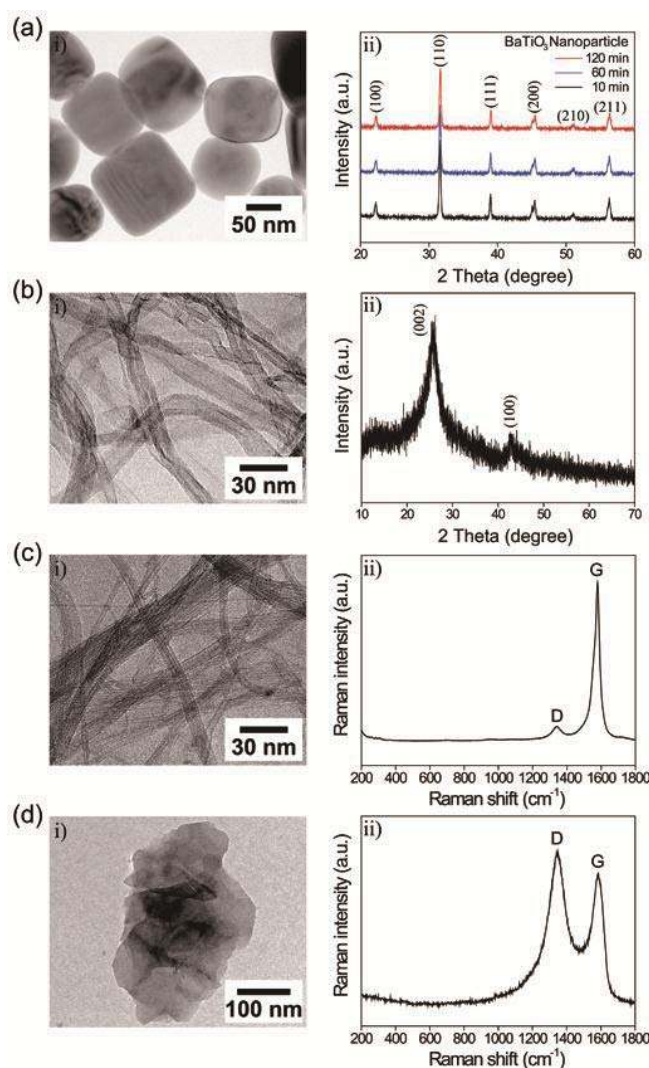
Figure S1. TEM images (left, i) of nanomaterials, XRD patterns (right, ii) of BaTiO₃ nanoparticles (NPs) (a), MW-CNTs (b) showing a diameter of ~ 20 nm, and Raman spectra (right, ii) of SW-CNTs (c) showing a diameter of ~ 3 nm, and reduced graphene oxide (RGO) (d). Raman spectra of the MW-CNTs (the inset of Figure 1e) and RGO (Figure S1d-ii) show quite large D bands because the graphite layers accommodate a high quantity of structural defects.[1-4] In contrast, the spectrum of SW-CNTs (Figure S1c-ii) has a sharp G band, which indicates the excellent crystallinity of the material. [2-4]

2. Fabrication process of bulk-type nanocomposite generator (NCG)
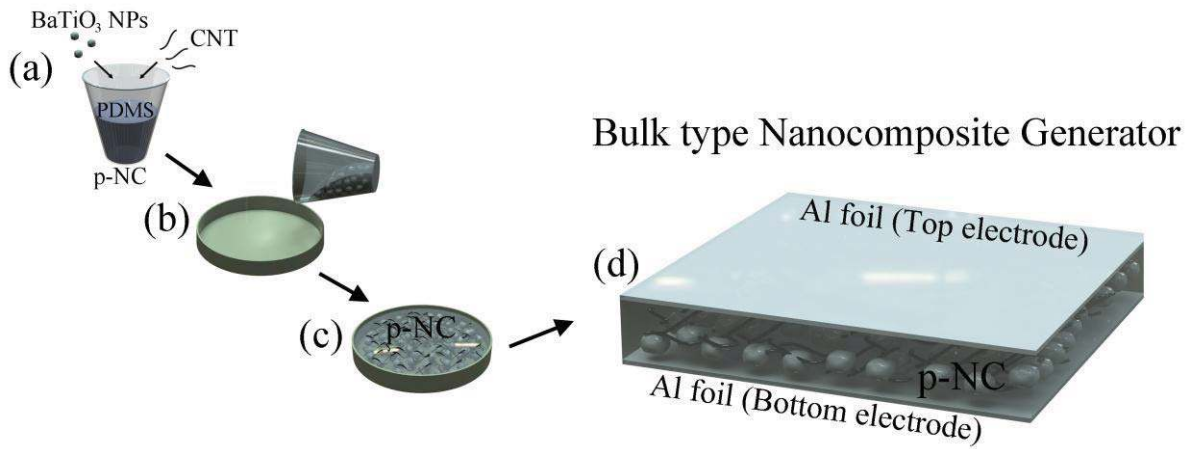
Figure S2. Schematic illustration of the process for fabricating NCG device. The p-PDMS containing the two nano-materials (a) is poured into a petri dish (b) and cured at room temperature for one day (c). The 'piezoelectric rubber' bulk-type NCG is wrapped with aluminum (Al) foils which are used to top/bottom electrodes (d).
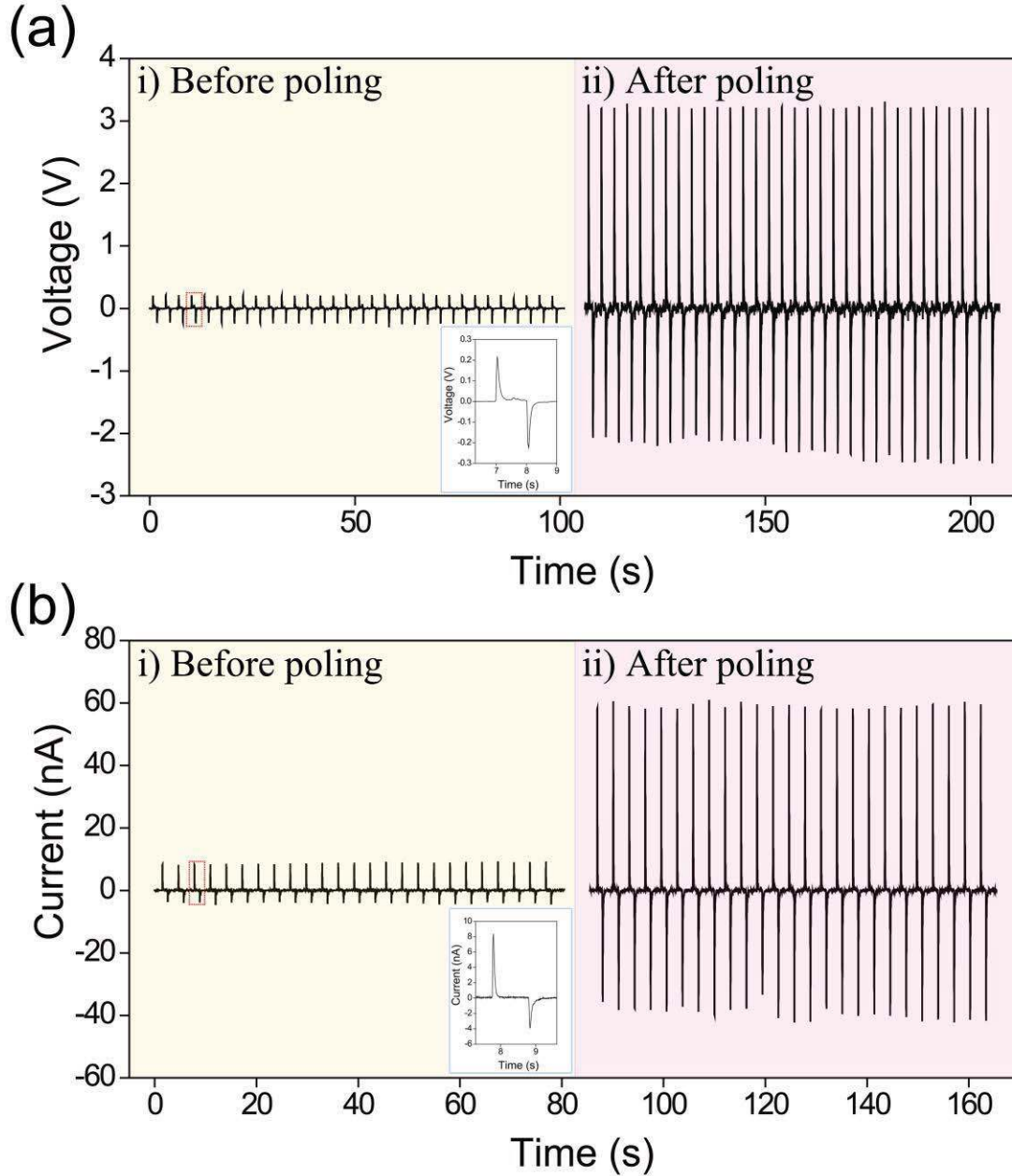
**3. The output voltage and current signals generated from bulk-type NCG device**
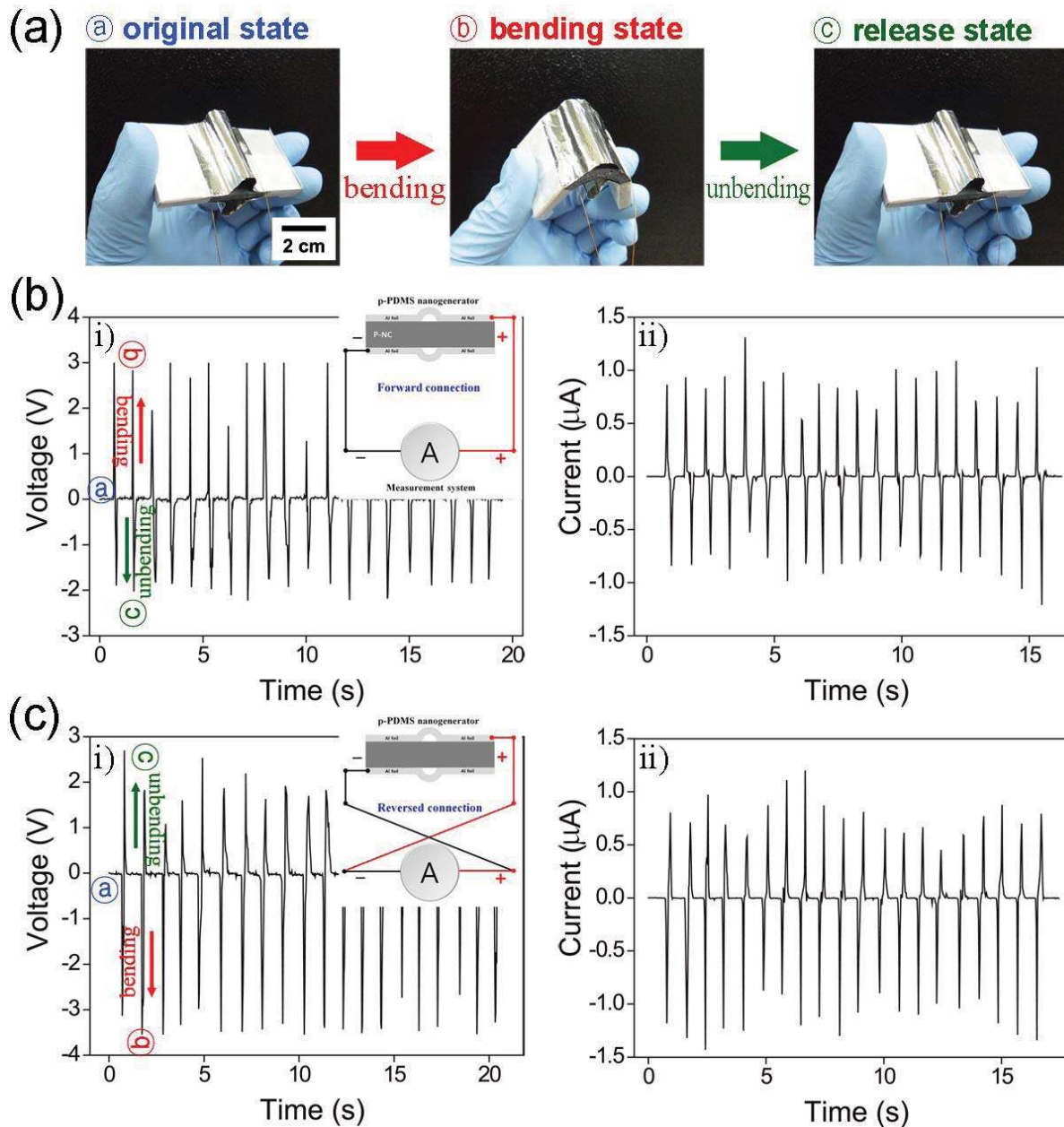
Figure S3. (a) Optical images of bulk-type NCG devices in original, bending, and release states. (b) The measured output voltage (left, i) and current signals (right, ii) of the bulk-type NCG device during periodically bending and unbending motion when forward-connected (corresponding to the inset of Figure S3b-i) to the measurement system. (c) The generated output voltage (left, i) and current signals (right, ii) in the case of the reverse connection (corresponding to the inset of Figure S3c-i).

4. The measured output voltage and current signals of NCG device before and after poling process

Figure S4. The output voltage (a) and current signals (b) generated from NCG devices before and after poling process. The generated output voltage and current signals are dramatically increased by poling process. The insets show the magnified output signals.

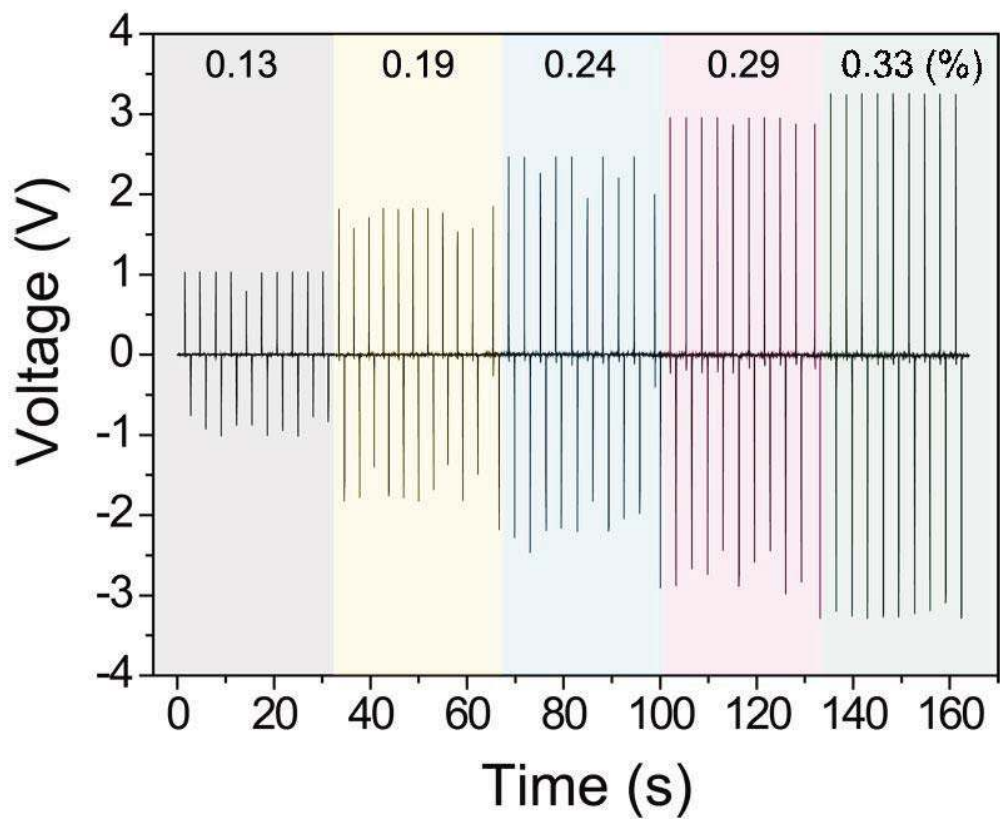**5. The output voltage of the NCG device containing the various compositions**
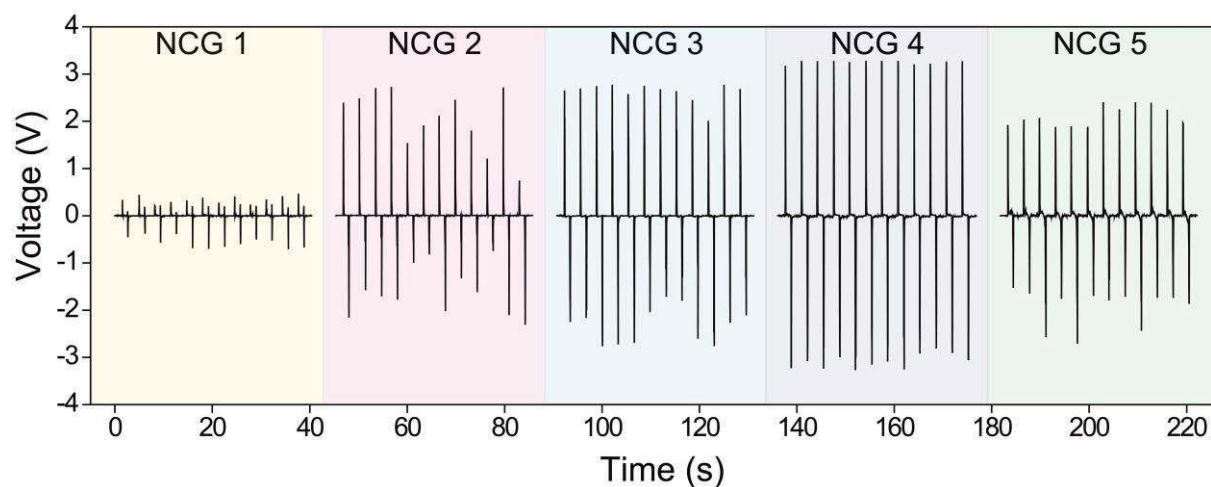
Figure S5. The output voltage of the NCG fabricated at various composition of $BaTiO_3$ NPs and MW-CNTs. The fabricated NCG devices had a composition varying from 6 to 20 wt% $BaTiO_3$ NPs; the designations of these devices are summarized in Table S1. The output voltage of NCG 4 shows high and uniform signals.

Table S1. Compositions and their designations.

| Composition	Designation
0.5 wt% MW-CNTs and 12 wt% $BaTiO_3$ NPs	NCG 1
1 wt% MW-CNTs and 6 wt% $BaTiO_3$ NPs	NCG 2
1 wt% MW-CNTs and 9 wt% $BaTiO_3$ NPs	NCG 3
1 wt% MW-CNTs and 12 wt% $BaTiO_3$ NPs	NCG 4
1 wt% MW-CNTs and 20 wt% $BaTiO_3$ NPs	NCG 5

6. Performance characterization of the NCG device with increasing strain

Figure S6. Output voltage measurement of the NCG device with strain from 0.13 % to

0.33 %.

7. The output voltage of the NCG device when subject to slow or fast mechanical deformations
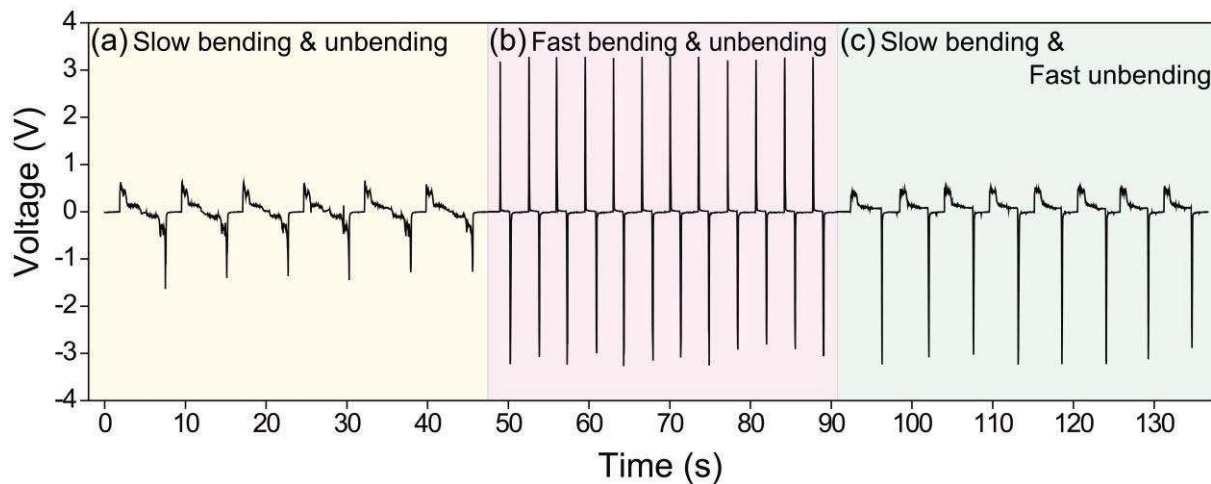
Figure S7. The output voltage generated from the NCG device when subject to periodical cycles of slow bending/unbending motions (a), fast bending/unbending motions (b), and slow bending/fast unbending motions (c).

8. The durability test of current signals generated from the NCG device
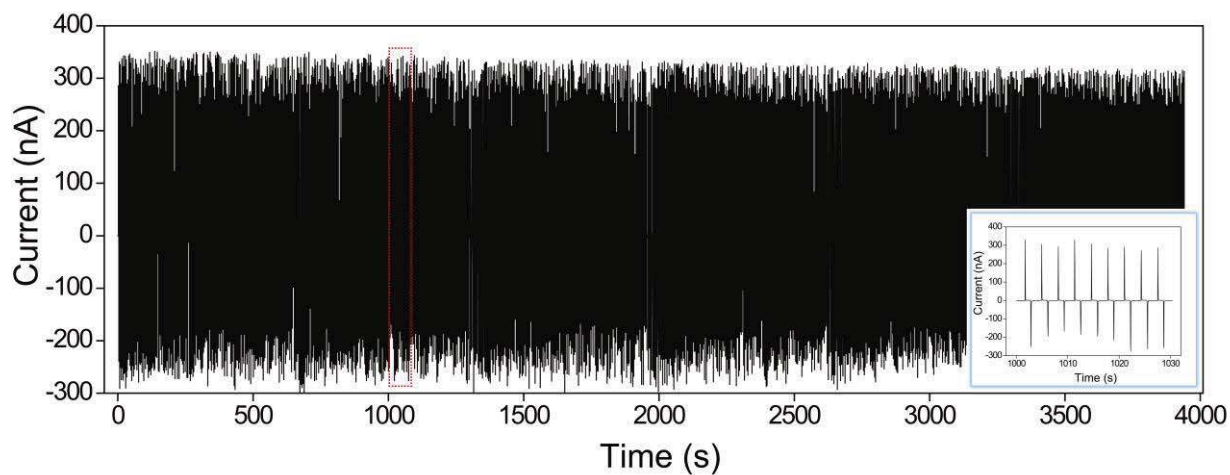
Figure S8. The durability test of current signals generated from NCG device. The amplitude of current signals does not appear the significant change upon periodically 1,200 bending cycles (during about 1 hour of operation).

## 9. The power generation mechanisms of the NCG device

The power generation mechanisms of the NCG device is described by the schematic diagram showing that the $BaTiO_3$ NPs generate the electric potential from external stress. Traditional piezoelectric ceramic materials (such as PZT and $BaTiO_3$) have a perovskite crystal structure.[5] Each crystal exhibits tetragonal or rhombohedral symmetry below the Curie temperature (approximately 130 ºC) and has a dipole moment that can be aligned by high electric fields. As shown in the cross-sectional structure of the poled NCG device in original state (without bending), almost all the domains that contain dipoles are arrayed in the direction of direct current electric fields. The top and bottom electrodes are connected with the positive and negative charges of the source meter, respectively. Even after the removal of the poling voltage, the rearranged domains maintain a permanent polarization (remanent polarization), which results in high piezoelectric properties with regard to the external stress. When the mechanical stress is applied on the NCG device by a bending motion, the positive and negative piezoelectric potentials are generated on the top and bottom of the p-NC due to the dipoles in the NPs. Note the strain neutral line is located at the substrate so that the entire composite is under tensile strain (see the details about calculation method and the true dimension of the device). The free electrons in the circuit have to flow through the external load to balance the field created by the NP dipoles, resulting in electric pulse in responding to the mechanical deformation. As the external pressure on the NCG device is removed by the unbending motion, the piezoelectric potential between the electrodes vanishes, and subsequently, the electrons accumulated at the top electrode flow back to the bottom side via the circuit, generating an electric pulse in the opposite direction. The mechanism presented here is similar to that reported by Hu et al. [6]
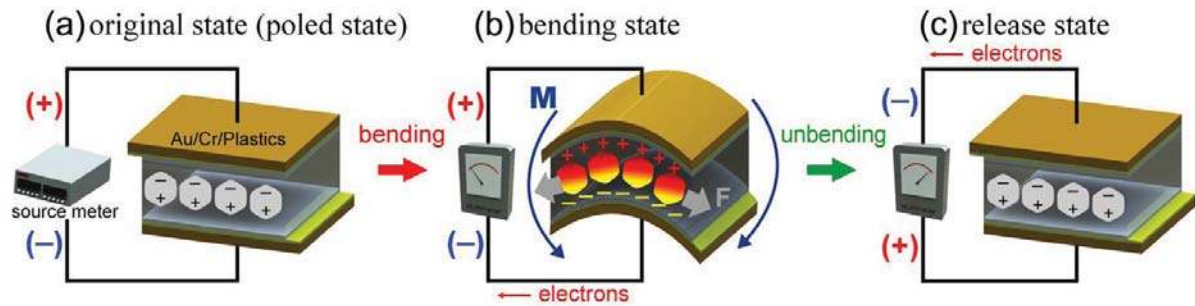
Figure S9. Schematics of the power generation mechanism of the NCG device. All dipoles are arrayed in the direction of the current electric fields in their original state without bending (a). When mechanical stress is applied to the NCG device by bending, the generated electrons can flow from the bottom electrode to the top electrode and generated an output voltage (b). In the case of the unbending state, the electrons accumulated at the top electrode move back to the bottom side and build up an electric pulse in the opposite direction (c).

**10. The voltage lifetime calculated from voltage-time plots**

(a)

(b)
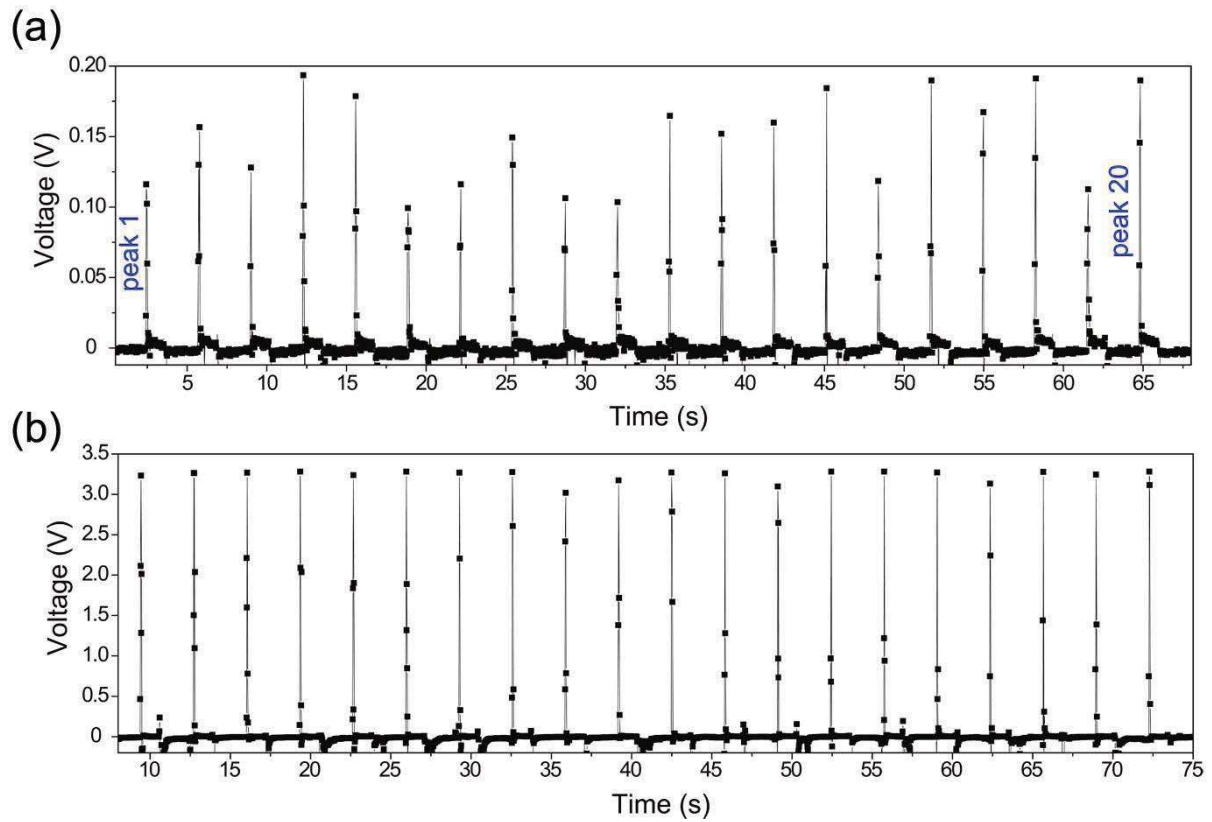
Figure S10. The voltage-time plots of device with only BaTiO$_3$ NPs (a) and NCG device (b). The voltage lifetime is defined as full width at half maximum (FWHM) of the voltage peaks which contain five data points.

15

Table S2. The calculated voltage lifetimes of device with only BaTiO$_3$ NPs and NCG device.

Device with only BaTiO$_3$ NPs				NCG device			
Peak No.	Voltage lifetime (ms)	Peak No.	Voltage lifetime (ms)	Peak No.	Voltage lifetime (ms)	Peak No.	Voltage lifetime (ms)
1	84.16	11	58.14	1	66.71	11	71.03
2	89.45	12	63.84	2	51.89	12	42.35
3	50.16	13	67.75	3	42.36	13	44.48
4	56.43	14	63.84	4	47.65	14	44.47
5	66.12	15	67.75	5	59.30	15	42.35
6	110.58	16	82.08	6	57.60	16	37.06
7	70.68	17	67.10	7	43.01	17	51.89
8	64.41	18	56.43	8	59.03	18	37.06
9	82.65	19	78.09	9	52.54	19	59.03
10	95.19	20	64.41	10	52.95	20	42.36
average lifetime (ms)		71.51		average lifetime (ms)		50.29	
standard deviation		15.18		standard deviation		9.58	

11. The comparison of the ouput voltages generated from a device containing only MW-CNT, only BaTiO₃ NPs , and a NCG device
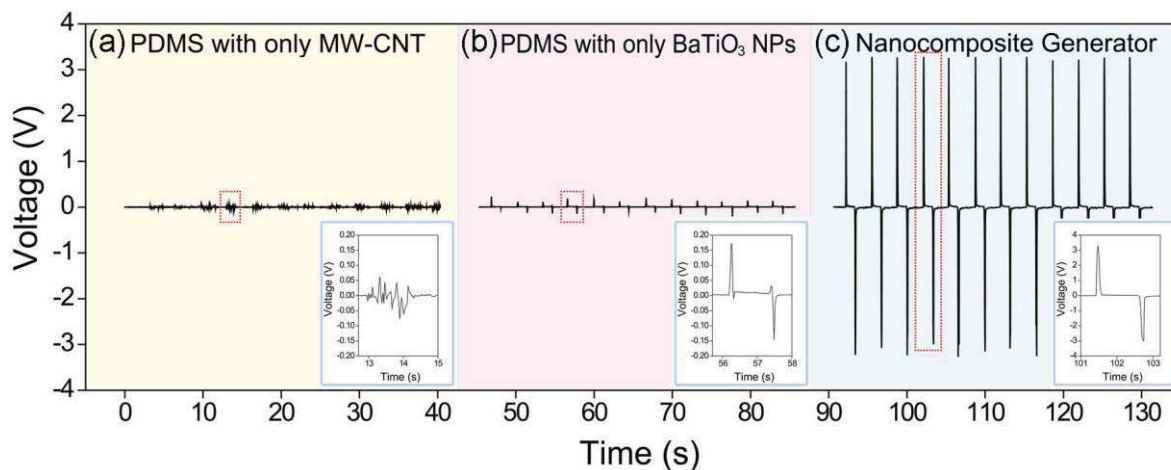
**Figure S11.** The output voltages generated from a device containing only MW-CNT (a), only BaTiO₃ NPs (b), and a NCG device (c). The bottom-right insets show the magnified output voltage generated by the mechanical deformations.

12. The measured output voltage from the NCG devices in which the MW-CNTs are replaced other graphitic carbons such as SW-CNTs or RGO
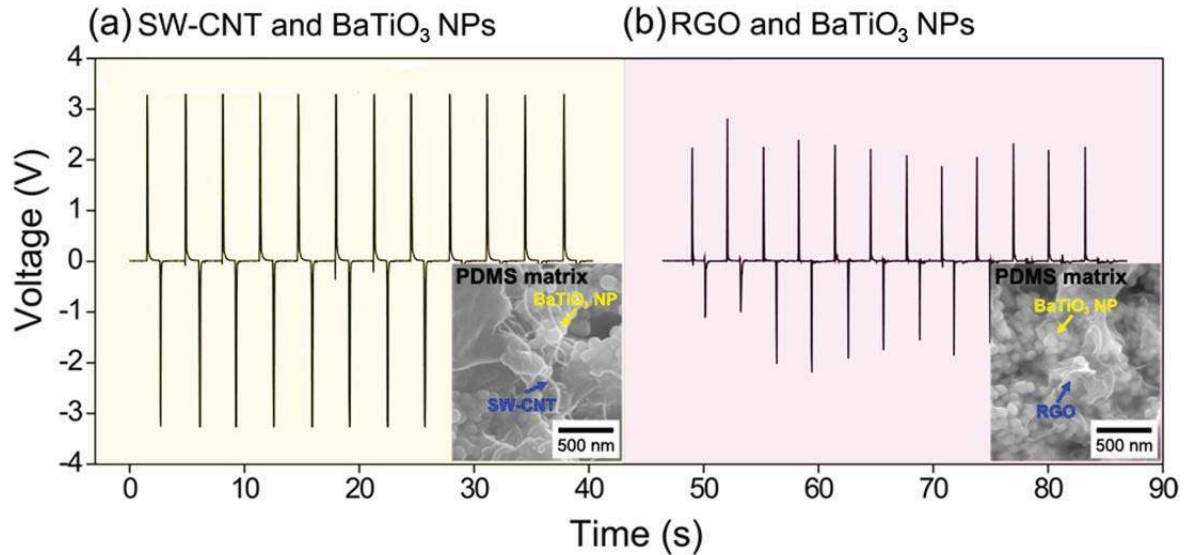
Figure S12. The measured output voltage from the NCG devices in which the MW-CNTs are replaced other graphitic carbons such as SW-CNTs (a) or RGO (b). The voltage of ~3.2 V generated from an SW-CNT-based NCG is very similar to that of the MW-CNT-based device; this result indicates that the electrical properties have no significant influence on the outputs. The low output voltage (~2.0 V) from the RGO-based NCG seems to be caused by the geometrical difference between the CNT networks and the RGO sheets. The insets show the cross-sectional SEM images of each device.

13. Energy conversion from human muscle movements
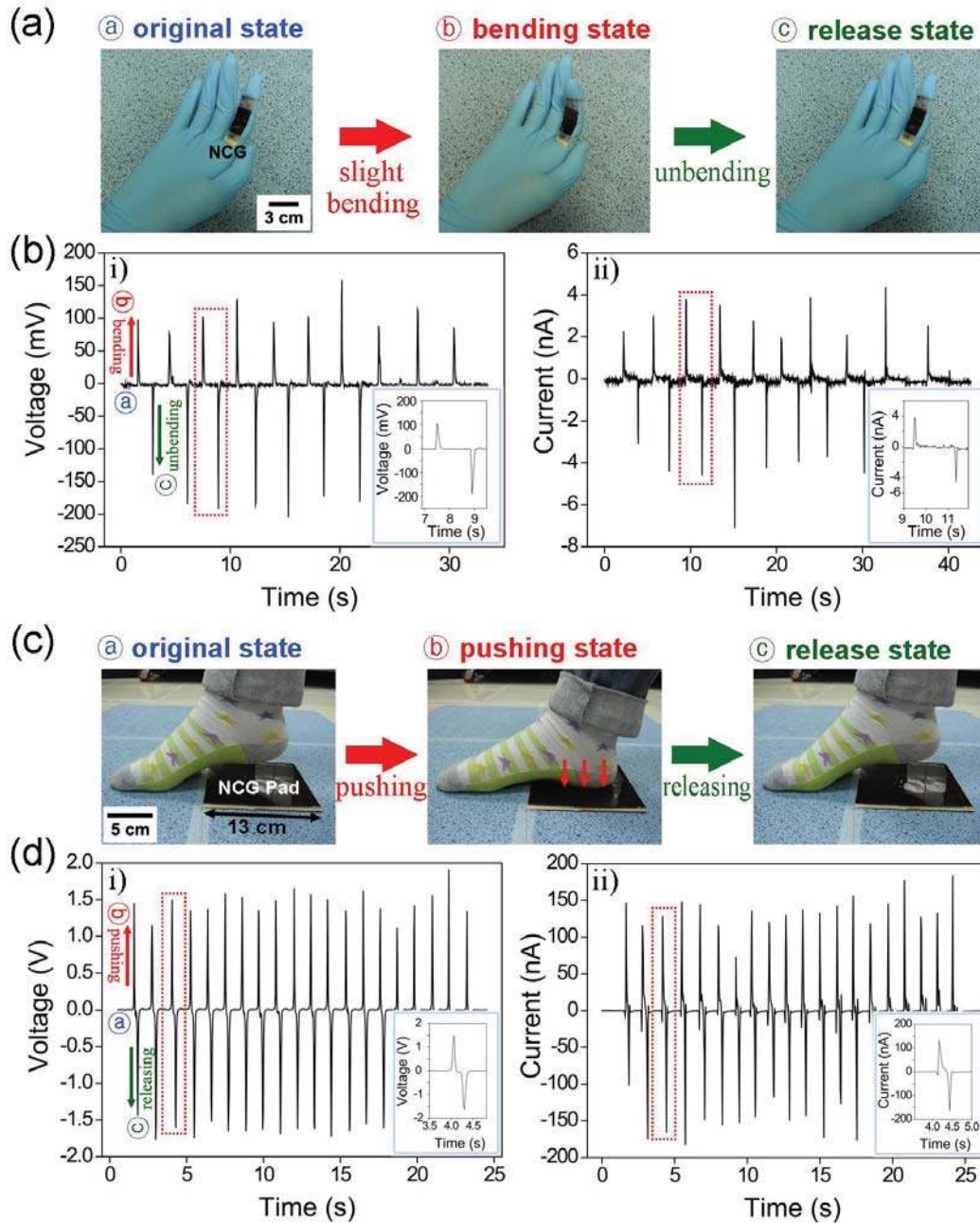
Figure S13. (a) A photograph of a small-scale NCG device (with an area of 1.5 cm x 4 cm) attached to a human finger in original, bending, and release states. (b) The output voltage (left, i) and current signals (right, ii) converted from the human finger motion. The bottom insets show the magnified output signals. (c) A photograph of a large-scale (13 cm x 13 cm) NCG pad in the original, pushing, and release states. (d) The generated output voltage (left, i) and current signals (right, ii) from human foot motion.

**14. Rectifying and charging circuit for a potential utilization of our energy harvesting technology**
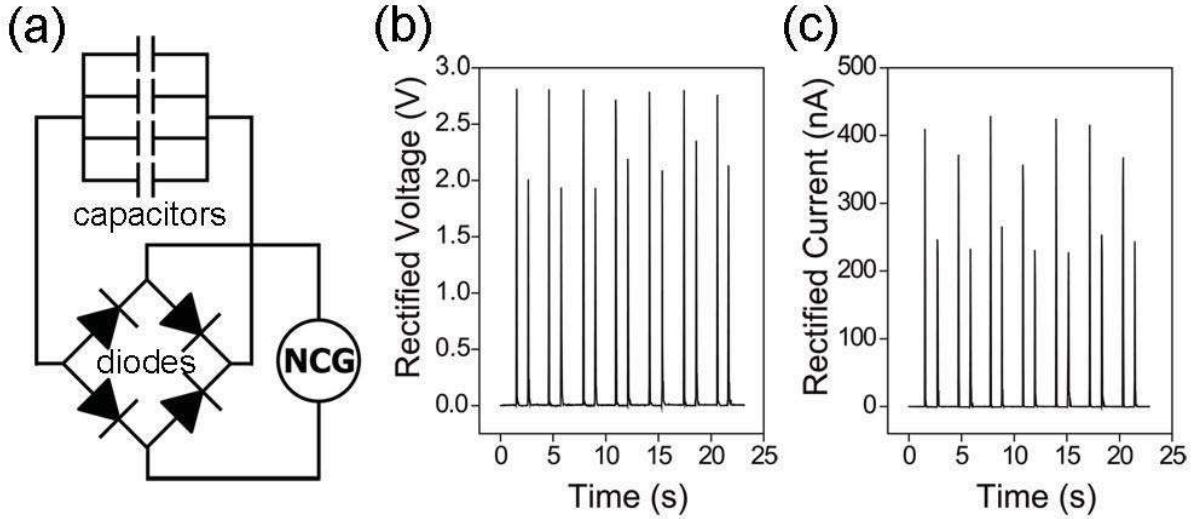
Figure S14. (a) A schematic diagram of the rectifying and charging circuit comprising four diodes and four capacitors; the capacitors are connected in parallel with the rectifying circuit. The measured output voltage (b) and current signals (c) after rectification.

Reference

[1] S. Costa, M. Kruszynska, A. Bachmatiuk, R. J. Kalenczuk, E. Borowiak-Palen, *Mater. Sci.-Poland* **2008**, *26*, 433.

[2] P. Delhaes, M. Couzi, M. Trinquecoste, J. Dentzer, H. Hamidou, C. Vix-Guterl, *Carbon* **2006**, *44*, 3005.

[3] S. Lee, J. W. Peng, C. H. Liu, *Carbon* **2009**, *47*, 3488.

[4] V. M. Irurzun, M. P. Ruiz, D. E. Resasco, *Carbon* **2010**, *48*, 2873.

[5] I. R. Henderson, *Piezoelectric Ceramics: Principles and Applications,* APC International, Pennsylvania, **2002**.

[6] Y. Hu, Y. Zhang, C. Xu, G. Zhu, Z. L. Wang, *Nano Lett.* **2010**, *10*, 5025.

Video
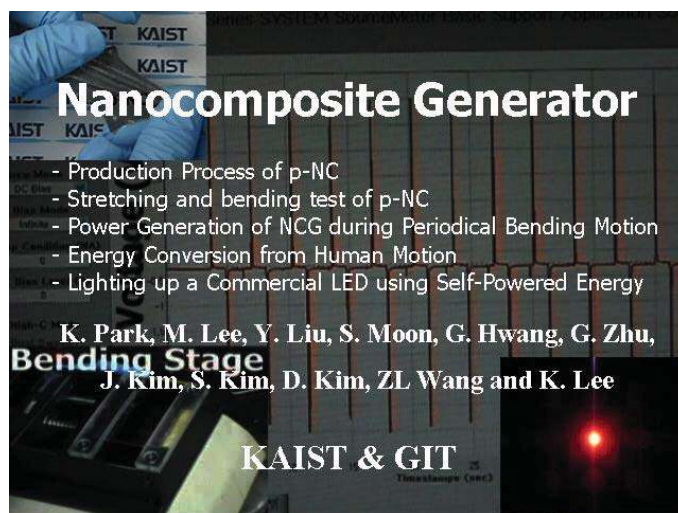
Video S1

Live video includes:

(a) Production process of piezoelectric nanocomposite (p-NC).

(b) Stretching and bending test of p-NC

(c) Power generation of NCG device during periodical bending motions by bending stage.

(d) Energy conversion from human finger and foot motions into electric energy.

(e) A commercial LED lit up by the energy generated from the NCG device.